Geophysical Journal International

Geophys. J. Int. (2014) **199,** 416–429
GJI Seismology

doi: 10.1093/gji/ggu272

Source spectra of seismic hum

Kiwamu Nishida

Earthquake Research Institute, University of Tokyo, Yayoi 1-1-1, *Bunkyo-ku, Tokyo* 113-0032, *Japan. E-mail: knishida@eri.u-tokyo.ac.jp*

Accepted 2014 July 14. Received 2014 June 27; in original form 2014 March 23

SUMMARY

The observation of seismic hum from 2 to 20 mHz, also known as Earth's background free oscillations, has been established. Recent observations by broad-band seismometers show simultaneous excitation of Love waves (fundamental toroidal modes) and Rayleigh waves (fundamental spheroidal modes). The excitation amplitudes above 10 mHz can be explained by random shear traction sources on Earth's surface. With estimated source distributions, the most likely excitation mechanism is a linear coupling between ocean infragravity waves and seismic surface waves through seafloor topography. Observed Love and Rayleigh wave amplitudes below 5 mHz suggest that surface pressure sources could also contribute to their excitations, although the amplitudes have large uncertainties due to the high noise levels of the horizontal components. To quantify the observation, we develop a new method for estimation of the source spectra of random tractions on Earth's surface by modelling cross-spectra between pairs of stations. The method is to calculate synthetic cross-spectra for spatially isotropic and homogeneous excitations by random shear traction and pressure sources, and invert them with the observed cross-spectra to obtain the source spectra. We applied this method to the IRIS, ORFEUS, and F-net records from 618 stations with three components of broad-band seismometers for 2004–2011. The results show the dominance of shear traction above 5 mHz, which is consistent with past studies. Below 5 mHz, however, the spectral amplitudes of the pressure sources are comparable to those of shear traction. Observed acoustic resonance between the atmosphere and the solid Earth at 3.7 and 4.4 mHz suggests that atmospheric disturbances are responsible for the surface pressure sources, although non-linear ocean wave processes are also candidates for the pressure sources. Excitation mechanisms of seismic hum should be considered as a superposition of the processes of the solid Earth, atmosphere and ocean as a coupled system.

Key words: Surface waves and free oscillations; Wave propagation.

1 INTRODUCTION

It has long been understood that only very large earthquakes and volcanic eruptions excite Earth's free oscillations at observable levels. In 1998, some Japanese groups discovered persistent excitation of normal modes in the mHz band even on seismically quiet days (Kobayashi & Nishida 1998; Nawa *et al.* 1998; Suda *et al.* 1998). They are known as seismic hum or background free oscillations. Currently at more than a hundred quiet broad-band stations, the power spectra of the vertical components exhibit many spectral peaks at eigenfrequencies of fundamental spheroidal modes (Nishida 2013a). The root mean squared amplitudes of each mode from 2 to 8 mHz are on the order of 0.5 nGal (10^{-11} m s^{-2}) with little frequency dependence. These observations show that the excitation sources are persistent disturbances distributed over Earth's entire surface.

To constrain their excitation mechanisms, source distributions of background Rayleigh waves were inferred from an array analysis of the vertical components of broad-band seismometers and a cross-correlation analysis of the signals. In the Northern Hemisphere winter, they were dominant in the northern Pacific Ocean, whereas in the Southern Hemisphere winter, they were dominant in the Antarctic Ocean (Rhie & Romanowicz 2004, 2006; Nishida & Fukao 2007; Bromirski & Gerstoft 2009; Traer *et al.* 2012). Throughout the years, excitation sources on the continents are too weak to detect. These results suggest that the activity of ocean infragravity waves is a dominant source of seismic hum (e.g. Watada & Masters 2001; Rhie & Romanowicz 2004; Webb 2007).

Observation of background Love waves (or background excitation of fundamental toroidal modes) is crucial for constraining the excitation mechanisms. Because the noise levels of the horizontal components are higher than those of the vertical components, background Love waves were detected at the four quietest sites by a single station analysis. Background Rayleigh and Love waves exhibit similar horizontal

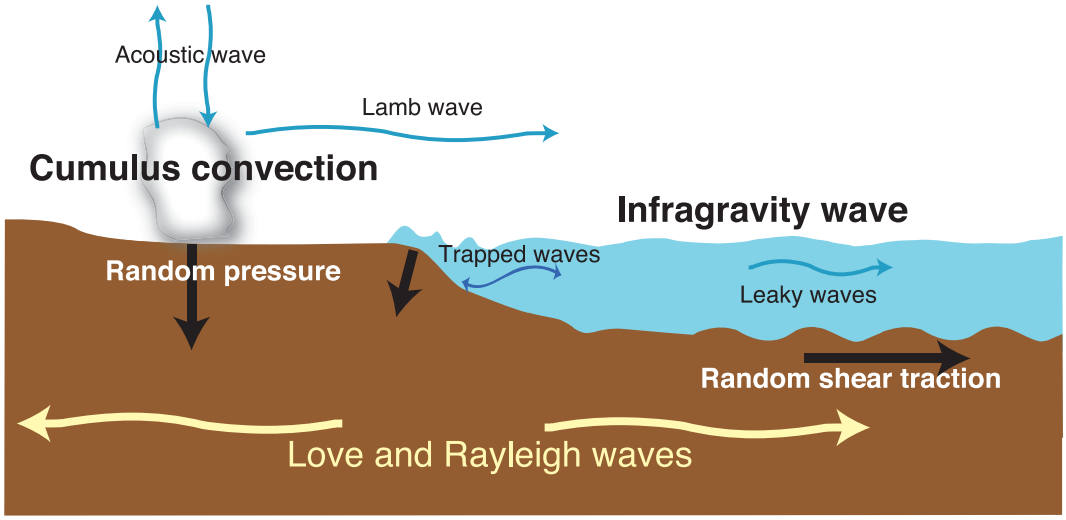

Figure 1. Schematic figure of possible excitation mechanisms of seismic hum.

amplitudes from 3.2 to 4.2 mHz (Kurrle & Widmer-Schnidrig 2008), although the estimated amplitude by the single station analysis had a large intrinsic uncertainty due to high noise levels of the horizontal components. In ten years, dense arrays of broad-band seismometers have been developed in the United States, Japan and Europe (e.g. USArray, Hi-net). Horizontal records from more than 500 stations enabled us to estimate precise amplitudes of the background Love and Rayleigh waves. A recent result by the array data showed that the observed kinetic energy of background Love waves was as large as that of background Rayleigh waves from 10 to 100 mHz (Nishida *et al.* 2008).

The excitation sources above 10 mHz can be represented by random shear traction on Earth's surface. The only possible excitation mechanism is topographic coupling between ocean infragravity waves and seismic surface waves (Nishida *et al.* 2008; Fukao *et al.* 2009; Saito 2010). Below 5 mHz, however, the shear traction sources overpredict Love wave amplitudes. They are much larger than the ones observed in the frequency range from 3 to 7 mHz (Kurrle & Widmer-Schnidrig 2008), although Rayleigh wave amplitudes are consistent with each other. To explain the amplitudes below 5 mHz, Fukao *et al.* (2009) suggested that pressure sources also contribute to the excitation below 5 mHz (Nishida 2013b). In this frequency range, the spectra of the vertical components show two resonant peaks at 3.7 and 4.4 mHz, corresponding to acoustic coupling modes between the solid Earth and the atmosphere (Nishida *et al.* 2000). This observation suggests that atmospheric disturbances also contribute to the excitation below 5 mHz as pressure sources (Fig. 1).

For a quantitative discussion on excitation mechanisms, we inferred the source spectra of the random pressure and shear traction on Earth's surface by modelling the cross-spectra between every pair of stations utilizing recent global data sets from broad-band seismometers. For the modelling, we developed a theory for a synthetic cross-spectrum between a pair of stations, assuming homogeneous and isotropic excitation sources, which are composed of random pressure sources and random shear traction sources on the whole Earth's surface. Then, we fit the synthetics to the observed cross-spectra to obtain the source spectra. Based on the source spectra, we will discuss two possible excitation mechanisms: (1) atmospheric disturbances and (2) non-linear effects of ocean infragravity waves at shallow depths and deep oceans.

2 A THEORY OF SYNTHETIC CROSS-SPECTRA BETWEEN A PAIR OF STATIONS

To synthesize a cross-spectrum between a pair of seismograms at stations $\boldsymbol{x}_1$ and $\boldsymbol{x}_2$ on Earth's surface, we consider a stochastic stationary wavefield excited by a random surface traction $\boldsymbol{\tau}$ acting upon a surface element $\mathrm{d}\Sigma$ at a point $\boldsymbol{x}$ on Earth's surface Σ. The displacement on Earth's surface $\boldsymbol{s}$ at location $\boldsymbol{x}$ and time t produced by such surface traction can be represented by convolution between the Green's function $\boldsymbol{g}$ and the surface traction $\boldsymbol{\tau}$ as

$$\boldsymbol{s}(\boldsymbol{x}, t) = \int_{-\infty}^{t} \int_{\Sigma} \boldsymbol{g}(\boldsymbol{x}, \boldsymbol{x}'; t - t') \cdot \boldsymbol{\tau}(\boldsymbol{x}'; t') \mathrm{d}\Sigma' \mathrm{d}t'. \tag{1}$$

The Green's function $\boldsymbol{g}$ for a spherical symmetric Earth can be written in terms of normal mode theory (Dahlen & Tromp 1998) as

$$\boldsymbol{g}(\boldsymbol{x}, \boldsymbol{x}'; t) = \sum_{nl} {}_n\gamma_l^S(t) \sum_m [{}_nU_l \boldsymbol{P}_{lm}(\hat{\boldsymbol{r}}) + {}_nV_l \boldsymbol{B}_{lm}(\hat{\boldsymbol{r}})][{}_nU_l \boldsymbol{P}_{lm}(\hat{\boldsymbol{r}}') + {}_nV_l \boldsymbol{B}_{lm}(\hat{\boldsymbol{r}}')] + \sum_{nl} {}_n\gamma_l^T(t) \sum_m {}_nW_l \boldsymbol{C}_{lm}(\hat{\boldsymbol{r}}) {}_nW_l \boldsymbol{C}_{lm}(\hat{\boldsymbol{r}}'), \tag{2}$$

where $\hat{\boldsymbol{r}}$ is a unit vector in the radial direction as shown in Fig. 2(a), ${}_nU_l$ is the vertical displacement of spheroidal modes on Earth's surface with a radial order n and an angular order l, ${}_nV_l$ is the horizontal displacement of the spheroidal mode and ${}_nW_l$ is the horizontal displacement of a toroidal mode. The modal oscillation ${}_n\gamma_l^M(t)$ is given by

$${}_n\gamma_l^M(t) = \begin{cases} \frac{\sin({}_n\omega_l^M t)}{{}_n\omega_k^M} \exp\left(-\frac{{}_n\omega_l^M}{2{}_nQ_l^M} t\right) & t \geq 0, \\ 0, & t < 0, \end{cases} \tag{3}$$

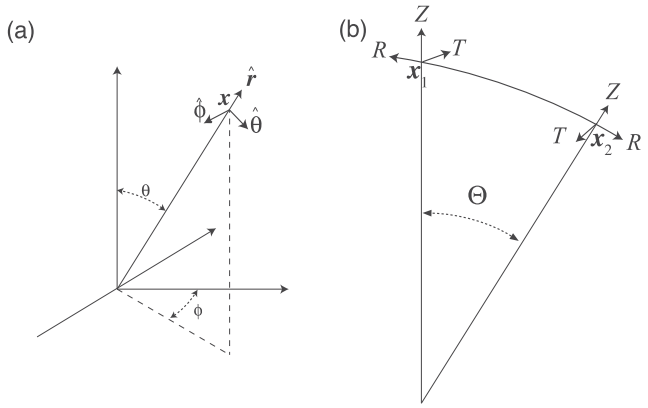

Figure 2. (a) Spherical coordinates used in this study. (b) Definition of radial (R), transverse (T) and vertical (Z) unit vectors at two stations ($\boldsymbol{x}_1, \boldsymbol{x}_2$). The radial direction is defined as that along the great circle path between the station pair. The transverse direction is defined as that perpendicular to the path. The angle between two stations is given by Θ.

where ${}_n\omega_l^M$ is the eigenfrequency of the mode, ${}_nQ_l^M$ is the quality factor of the mode and M represents the mode type (S: a spheroidal mode or T: a toroidal mode). $\boldsymbol{P}_{lm}$, $\boldsymbol{B}_{lm}$ and $\boldsymbol{C}_{lm}$ are vector spherical harmonics, defined as

$$\boldsymbol{P}_{lm} = \hat{\boldsymbol{r}}\mathcal{Y}_{lm}, \tag{4}$$

$$\boldsymbol{B}_{lm} = \frac{\nabla_1\mathcal{Y}_{lm}}{\sqrt{l(l+1)}} = \frac{[\hat{\boldsymbol{\theta}}\partial_\theta + \hat{\boldsymbol{\phi}}(\sin\theta)^{-1}\partial_\phi]\mathcal{Y}_{lm}}{\sqrt{l(l+1)}} \tag{5}$$

$$\boldsymbol{C}_{lm} = \frac{-\hat{\boldsymbol{r}}\times\nabla_1\mathcal{Y}_{lm}}{\sqrt{l(l+1)}} = \frac{[\hat{\boldsymbol{\theta}}(\sin\theta)^{-1}\partial_\phi - \hat{\boldsymbol{\phi}}\partial_\theta]\mathcal{Y}_{lm}}{\sqrt{l(l+1)}}, \tag{6}$$

where $\mathcal{Y}_{lm}$ are real spherical harmonics of angular order l and azimuthal order m (Dahlen & Tromp 1998), θ is the angle between $\boldsymbol{x}$ and the pole in spherical coordinates, and ϕ is the azimuth. The vectors $\hat{\boldsymbol{\theta}}$ and $\hat{\boldsymbol{\phi}}$ are corresponding unit vectors in horizontal directions, as shown in Fig. 2(a). In this study, we used a spherical symmetric earth model, PREM (Dziewonski & Anderson 1981) to calculate the eigenfrequencies and eigenfunctions.

With the above representations of random wavefields, we evaluated a cross-spectrum between a pair of seismograms at $\boldsymbol{x}_1$ and $\boldsymbol{x}_2$. A cross-spectrum $\Phi_{\alpha\beta}$ between an $\alpha(=r, \theta, \text{or } \phi)$ component of displacement at $\boldsymbol{x}_1$ and a β one at $\boldsymbol{x}_2$ is evaluated by

$$\Phi_{\alpha\beta}(\boldsymbol{x}_1, \boldsymbol{x}_2; \omega) = \int_{-\infty}^{\infty} \phi_{\alpha\beta}(\boldsymbol{x}_1, \boldsymbol{x}_2; t)\mathrm{e}^{-\mathrm{i}\omega t}\mathrm{d}t, \tag{7}$$

where ω is angular frequency, and the cross-correlation function $\phi_{\alpha\beta}$ between stations at $\boldsymbol{x}_1$ and $\boldsymbol{x}_2$ is defined by

$$\phi_{\alpha\beta}(\boldsymbol{x}_1, \boldsymbol{x}_2; t) = \lim_{T\to\infty}\frac{1}{T}\int_{-\frac{T}{2}}^{\frac{T}{2}} s_\alpha(\boldsymbol{x}_1, t')s_\beta(\boldsymbol{x}_2, t'+t)\mathrm{d}t'. \tag{8}$$

Insertion of eq. (1) into the above equation yields

$$\Phi_{\alpha\beta}(\boldsymbol{x}_1, \boldsymbol{x}_2; \omega) = \sum_{\alpha'\beta'}\iint_{\Sigma}\mathrm{d}\Sigma'\mathrm{d}\Sigma''\Psi_{\alpha'\beta'}(\boldsymbol{x}', \boldsymbol{x}''; \omega)G^*_{\alpha\alpha'}(\boldsymbol{x}_1, \boldsymbol{x}'; \omega)G_{\beta\beta'}(\boldsymbol{x}_2, \boldsymbol{x}''; \omega), \tag{9}$$

where $G_{\alpha\alpha'}(\boldsymbol{x}, \boldsymbol{x}'; \omega)$ is a Fourier component of the Green's function, which represents an α component of displacement at $\boldsymbol{x}$ for an impulsive force at $\boldsymbol{x}'$ with an α' component and $\Psi_{\alpha\beta}(\boldsymbol{x}, \boldsymbol{x}'; \omega)$ is a cross-spectrum between an α component of surface traction at $\boldsymbol{x}$ and a β component at $\boldsymbol{x}'$ given by

$$\Psi_{\alpha\beta}(\boldsymbol{x}', \boldsymbol{x}''; \omega) = \int_{-\infty}^{\infty}\psi_{\alpha\beta}(\boldsymbol{x}', \boldsymbol{x}''; t)\mathrm{e}^{-\mathrm{i}\omega t}\mathrm{d}t, \tag{10}$$

where a cross-correlation function $\psi_{\alpha\beta}$ of surface traction between $\boldsymbol{x}'$ and $\boldsymbol{x}''$ is given by

$$\psi_{\alpha\beta}(\boldsymbol{x}', \boldsymbol{x}''; t) = \lim_{T\to\infty}\frac{1}{T}\int_{-\frac{T}{2}}^{\frac{T}{2}}\tau_\alpha(\boldsymbol{x}', t')\tau_\beta(\boldsymbol{x}'', t+t')\mathrm{d}t', \tag{11}$$

where τ_α and τ_β represent components of traction (τ_r, τ_θ, τ_ϕ) on Earth's surface. Assuming that the surface traction is homogeneous and isotropic, we express the cross-spectral density of the surface traction as a simplified form of variable separation,

$$\Psi_{\alpha\beta}(\boldsymbol{x}', \boldsymbol{x}''; \omega) = \begin{cases}\Psi^0_{\alpha\beta}(\omega)\rho(\boldsymbol{x}', \boldsymbol{x}''; \omega), & \alpha = \beta,\\ 0, & \alpha \neq \beta,\end{cases} \tag{12}$$

where ρ is a structure function, and $\Psi^0_{\alpha\beta}(\omega)$ is the power spectral density (PSD) of surface traction of an $\alpha\beta$ component. The function $\rho(\boldsymbol{x}', \boldsymbol{x}''; \omega)$ is characterized by the frequency dependent correlation length $L(\omega)$ of the traction sources,

$$\rho(\boldsymbol{x}', \boldsymbol{x}''; \omega) = \begin{cases} 1, & x < L(\omega), \\ 0, & x \geq L(\omega). \end{cases} \tag{13}$$

Because L is estimated to be much smaller than the wavelengths of normal modes on the order of 1000 km (Fukao *et al.* 2002; Webb 2007), we can approximate the integral by Σ'' in eq. (9) by L^2 as

$$\begin{aligned} \Phi_{\alpha\beta}(\boldsymbol{x}_1, \boldsymbol{x}_2; \omega) &\sim L^2 \sum_{\alpha'\beta'} \int_\Sigma \mathrm{d}\Sigma' \Psi^e_{\alpha'\beta'}(\omega) G^*_{\alpha\alpha'}(\boldsymbol{x}_1, \boldsymbol{x}'; \omega) G_{\beta\beta'}(\boldsymbol{x}_2, \boldsymbol{x}'; \omega) \\ &= 4\pi^2 R_e^2 \sum_{\alpha'\beta'} \int_\Sigma \mathrm{d}\Sigma' \Psi^e_{\alpha'\beta'}(\omega) G^*_{\alpha\alpha'}(\boldsymbol{x}_1, \boldsymbol{x}'; \omega) G_{\beta\beta'}(\boldsymbol{x}_2, \boldsymbol{x}'; \omega), \end{aligned} \tag{14}$$

where R_e is Earth's radius, and the effective surface traction $\Psi^e_{\alpha\beta}(\omega)$ (Nishida & Fukao 2007) is defined as

$$\Psi^e_{\alpha\beta}(\omega) \equiv \frac{L^2(\omega)}{4\pi R_e^2} \Psi^0_{\alpha\beta}(\omega). \tag{15}$$

The effective traction can be written as

$$\Psi^e_{\alpha\beta}(\boldsymbol{x}; \omega) = \begin{cases} \bar{\Psi}^p(\omega) \Psi^e_{\mathrm{ref}}(\omega) & \alpha = \beta = r \\ \bar{\Psi}^t(\omega) \Psi^e_{\mathrm{ref}}(\omega) & \alpha = \beta = \theta \text{ or } \alpha = \beta = \phi \\ 0 & \text{otherwise}, \end{cases} \tag{16}$$

where $\bar{\Psi}^p(\omega)$ is the normalized effective pressure, and $\bar{\Psi}^t(\omega)$ is the normalized effective shear traction. We normalized them by a reference model of effective traction $\Psi^e_{ref}(\omega)$ based on the empirical model by Fukao *et al.* (2002). The reference model is expressed as

$$\Psi^e_{ref}(\omega) = \frac{2 \times 10^9}{4\pi R_e^2} \left(\frac{f}{f_0} \right)^{-2.3} (\mathrm{Pa}^2\,\mathrm{Hz}^{-1}), \tag{17}$$

where the reference frequency f_0 is 1 mHz. The random surface-pressure source given by the reference model explains the observed Rayleigh wave amplitudes of seismic hum at frequencies below 6 mHz, which will be modified so that it can explain the higher frequency data including Love wave amplitudes as well. We note that the normalized effective pressure $\bar{\Psi}^p(\omega)$ and the normalized effective shear traction $\bar{\Psi}^t(\omega)$ are real functions because the definition of $\Psi^e_{\alpha\beta}$ yields the Hermitian relation as $\Psi^e_{\alpha\beta}(\omega) = \Psi^{e*}_{\beta\alpha}(\omega)$.

Given the orthogonality relation of the vector spherical harmonics:

$$\begin{aligned} &\int_\Sigma \mathrm{d}\Sigma \boldsymbol{P}_{lm}(\hat{\boldsymbol{r}}) \cdot \boldsymbol{P}_{l'm'}(\hat{\boldsymbol{r}}) = R_e^2 \delta_{ll'} \delta_{mm'}, \quad \int_\Sigma \mathrm{d}\Sigma \boldsymbol{P}_{lm}(\hat{\boldsymbol{r}}) \cdot \boldsymbol{B}_{l'm'}(\hat{\boldsymbol{r}}) = 0, \\ &\int_\Sigma \mathrm{d}\Sigma \boldsymbol{B}_{lm}(\hat{\boldsymbol{r}}) \cdot \boldsymbol{B}_{l'm'}(\hat{\boldsymbol{r}}) = R_e^2 \delta_{ll'} \delta_{mm'}, \quad \int_\Sigma \mathrm{d}\Sigma \boldsymbol{P}_{lm}(\hat{\boldsymbol{r}}) \cdot \boldsymbol{C}_{l'm'}(\hat{\boldsymbol{r}}) = 0, \\ &\int_\Sigma \mathrm{d}\Sigma \boldsymbol{C}_{lm}(\hat{\boldsymbol{r}}) \cdot \boldsymbol{C}_{l'm'}(\hat{\boldsymbol{r}}) = R_e^2 \delta_{ll'} \delta_{mm'}, \quad \int_\Sigma \mathrm{d}\Sigma \boldsymbol{B}_{lm}(\hat{\boldsymbol{r}}) \cdot \boldsymbol{C}_{l'm'}(\hat{\boldsymbol{r}}) = 0. \end{aligned} \tag{18}$$

We insert eqs (2) and (16) into eq. (14) to obtain the representation of the synthetic cross-spectrum as

$$\begin{pmatrix} \Phi_{ZZ}(\Theta, \omega) & \Phi_{RZ}(\Theta, \omega) & \Phi_{TZ}(\Theta, \omega) \\ \Phi_{ZR}(\Theta, \omega) & \Phi_{RR}(\Theta, \omega) & \Phi_{TR}(\Theta, \omega) \\ \Phi_{ZT}(\Theta, \omega) & \Phi_{RT}(\Theta, \omega) & \Phi_{TT}(\Theta, \omega) \end{pmatrix} = {}^t\boldsymbol{R}_1 \begin{pmatrix} \Phi_{rr}(\Theta, \omega) & \Phi_{\theta r}(\Theta, \omega) & \Phi_{\phi r}(\Theta, \omega) \\ \Phi_{r\theta}(\Theta, \omega) & \Phi_{\theta\theta}(\Theta, \omega) & \Phi_{\phi\theta}(\Theta, \omega) \\ \Phi_{r\phi}(\Theta, \omega) & \Phi_{\theta\phi}(\Theta, \omega) & \Phi_{\phi\phi}(\Theta, \omega) \end{pmatrix} {}^t\boldsymbol{R}_2, \tag{19}$$

where Θ is the separation angular distance between the pair of stations, and we define radial (R), transverse (T) and vertical (Z) components for the station pair as shown in Fig. 2(b), $\boldsymbol{R}_1$ is the rotation matrix at $\boldsymbol{x}_1$ from spherical coordinates to the station-station coordinates, and $\boldsymbol{R}_2$ is that at $\boldsymbol{x}_2$, the superscript t represents the transpose (see Appendix for details). The *RR*, *TT*, *ZZ*, *RZ* and *ZR* components of the synthetic cross spectra can be written as functions of only Θ and ω,

$$\Phi_{ZZ}(\Theta, \omega) = \sum_l P_l(\cos\Theta) [\zeta^p_{l,ZZ}(\omega) \bar{\Psi}^p(\omega) + \zeta^t_{l,ZZ}(\omega) \bar{\Psi}^t(\omega)],$$

$$\Phi_{RR}(\Theta, \omega) = \sum_l \frac{P_l''(\cos\Theta)}{k^2} [\zeta^p_{l,RR}(\omega) \bar{\Psi}^p(\omega) + \zeta^t_{l,RR}(\omega) \bar{\Psi}^t(\omega)] + \sum_l \frac{P_l'(\cos\Theta)}{k^2 \sin\theta} \zeta^t_{l,TT}(\omega) \bar{\Psi}^t(\omega),$$

$$\Phi_{TT}(\Theta, \omega) = \sum_l \frac{P_l'(\cos\Theta)}{k^2 \sin\theta} [\zeta^p_{l,RR}(\omega) \bar{\Psi}^p(\omega) + \zeta^t_{l,RR}(\omega) \bar{\Psi}^t(\omega)] + \sum_l \frac{P_l''(\cos\Theta)}{k^2} \zeta^t_{l,TT}(\omega) \bar{\Psi}^t(\omega),$$

$$\Phi_{ZR}(\Theta,\omega) = \Phi^{*}_{RZ}(\Theta,\omega) = \sum_{l} \frac{P_l'(\cos\Theta)}{k}[\zeta^{p}_{l,RZ}(\omega)\bar{\Psi}^{p}(\omega) + \zeta^{t}_{l,RZ}(\omega)\bar{\Psi}^{t}(\omega)],$$

$$\Phi_{TZ}(\Theta,\omega) = \Phi_{ZT}(\Theta,\omega) = \Phi_{RT}(\Theta,\omega) = \Phi_{TR}(\Theta;\omega) = 0, \tag{20}$$

where the primes ($'$) as in P' or P'' indicate spatial derivatives with respect to Θ. Here, $\zeta^{p}_{l,\alpha\beta}(\omega)$ and $\zeta^{t}_{l,\alpha\beta}(\omega)$ are the frequency wavenumber (FK) spectra of an $\alpha\beta$ component (α, $\beta = R, T, Z$) defined as

$$\zeta^{p}_{l,ZZ}(\omega) = \pi R_e^4(2l+1)\Psi^{e}_{\mathrm{ref}}(f)\sum_{nn'} {}_n\Gamma^{S}_{l}(\omega)_{n'}\Gamma^{S*}_{l}(\omega)_n U^2_{l\,n'}U^2_l,$$

$$\zeta^{t}_{l,ZZ}(\omega) = \pi R_e^4(2l+1)\Psi^{e}_{\mathrm{ref}}(f)\sum_{nn'} {}_n\Gamma^{S}_{l}(\omega)_{n'}\Gamma^{S*}_{l}(\omega)_n U_{ln'}U_{ln}V_{ln'}V_l,$$

$$\zeta^{p}_{l,RR}(\omega) = \pi R_e^4(2l+1)\Psi^{e}_{\mathrm{ref}}(f)\sum_{nn'} {}_n\Gamma^{S}_{l}(\omega)_{n'}\Gamma^{S*}_{l}(\omega)_n U_{ln'}U_{ln}V_{ln'}V_l,$$

$$\zeta^{t}_{l,RR}(\omega) = \pi R_e^4(2l+1)\Psi^{e}_{\mathrm{ref}}(f)\sum_{nn'} {}_n\Gamma^{S}_{l}(\omega)_{n'}\Gamma^{S*}_{l}(\omega)_n V^2_{l\,n'}V^2_l,$$

$$\zeta^{t}_{l,TT}(\omega) = \pi R_e^4(2l+1)\Psi^{e}_{\mathrm{ref}}(f)\sum_{nn'} {}_n\Gamma^{T}_{l}(\omega)_{n'}\Gamma^{T*}_{l}(\omega)_n W^2_{l\,n'}W^2_l,$$

$$\zeta^{p}_{l,ZR}(\omega) = \pi R_e^4(2l+1)\Psi^{e}_{\mathrm{ref}}(f)\sum_{nn'} {}_n\Gamma^{S}_{l}(\omega)_{n'}\Gamma^{S*}_{l}(\omega)_n U^2_{l\,n'}U_{ln'}V_l,$$

$$\zeta^{t}_{l,ZR}(\omega) = \pi R_e^4(2l+1)\Psi^{e}_{\mathrm{ref}}(f)\sum_{nn'} {}_n\Gamma^{S}_{l}(\omega)_{n'}\Gamma^{S*}_{l}(\omega)_n U_{ln}V_{ln'}V^2_l, \tag{21}$$

where the ζ superscripts p and t represent pressure and shear traction sources, respectively, and $\Gamma^{M}_{l}(\omega)$ is the Fourier component of $\gamma^{M}_{l}(\omega)$:

$${}_n\Gamma^{M}_{l}(\omega) = \frac{1}{\left[-\frac{{}_n\omega^{M}_{l}}{2{}_nQ^{M}_{l}} - \mathrm{i}({}_n\omega^{M}_{l} - \omega)\right]\left[-\frac{{}_n\omega^{M}_{l}}{2{}_nQ^{M}_{l}} + \mathrm{i}({}_n\omega^{M}_{l} + \omega)\right]}. \tag{22}$$

The cross-spectra Φ_{ZZ} and Φ_{ZR} are directly related to the corresponding FK spectra, whereas Φ_{RR} and Φ_{TT} have cross-talk terms with each other. For example, Φ_{RR} contains three terms of ζ^{p}_{RR}, ζ^{t}_{RR} and ζ^{t}_{TT} as shown in eq. (20). The Rayleigh wave (the first two terms) decay with separation distance Θ as $P_l''(\cos\Theta) \sim [\sin\Theta]^{-1/2}$ in the regime $0 \ll \Theta \ll \pi$, whereas the Love wave (the third term) decays as $P_l'(\cos\Theta)/\sin\Theta \sim [\sin\Theta]^{-3/2}$. This means that the contribution of the Love wave (the cross-talk term) decays with separation distance more rapidly than that of the Rayleigh wave. This cross-talk term becomes comparable to the Rayleigh wave term when the separation distance is shorter than the wavelength of the surface waves.

Figs 3(b) and (c) show the synthetic FK spectra ($\zeta^{p}_{l,\alpha\beta}$ and $\zeta^{t}_{l,\alpha\beta}$) against angular orders and frequencies. For comparison with observed FK spectra, we take into account the effect of data tapering. This effect is given by convolution with the PSD of the taper function (the Welch window function in this study). The spectra of the *ZZ*, *RR* and the real part ($\Re$) of *ZR* show a clear Rayleigh wave branch (the fundamental spheroidal mode), whereas the *TT* spectrum shows a Love wave branch (fundamental toroidal mode). Lack of the *TT* component for a pressure source means that the pressure source cannot, in principle, excite toroidal modes.

The FK spectrum of the *RR* component for the pressure source lacks overtones, whereas that for the shear traction source shows a clear overtone branch corresponding to the shear-coupled PL wave in the temporal-spatial domain (Nishida 2013b). The FK spectrum of the *ZZ* component of the pressure source shows many different overtones associated with teleseismic body waves corresponding to direct *P*, *PP*, *PPP*, *PcP* waves, etc.

We note that the synthetic FK spectra of the *ZZ*, *RR* and *TT* components have only real components. On the other hand, that of the *ZR* component has both real and imaginary components. This difference comes from coupling between modes with the same angular orders *l* but different radial orders *n*. The imaginary parts of the *ZZ*, *RR* and *TT* components are cancelled out because of the symmetry between *n* and n'. However, the imaginary part of the *ZR* component remains, although the amplitude is smaller than that of the real part. The coupling becomes important when we discuss details of body wave propagation at a higher frequency (Takagi *et al.* 2014) because their mode spacings become dense.

3 OBSERVATION

We analysed continuous sampling records from 2004 to 2011 at 618 stations (Fig. 4a) with three components of broad-band seismometers (STS-1, STS2 and STS2.5) at the lowest ground noise levels (Peterson 1993; Berger *et al.* 2004; Nishida 2013b). We used data obtained from the International Federation of Digital Seismographic Networks (FSDN), Observatories and Research Facilities for European Seismology (ORFEUS) and F-net stations of the National Research Institute for Earth Science and Disaster Prevention (NIED). For each station, the

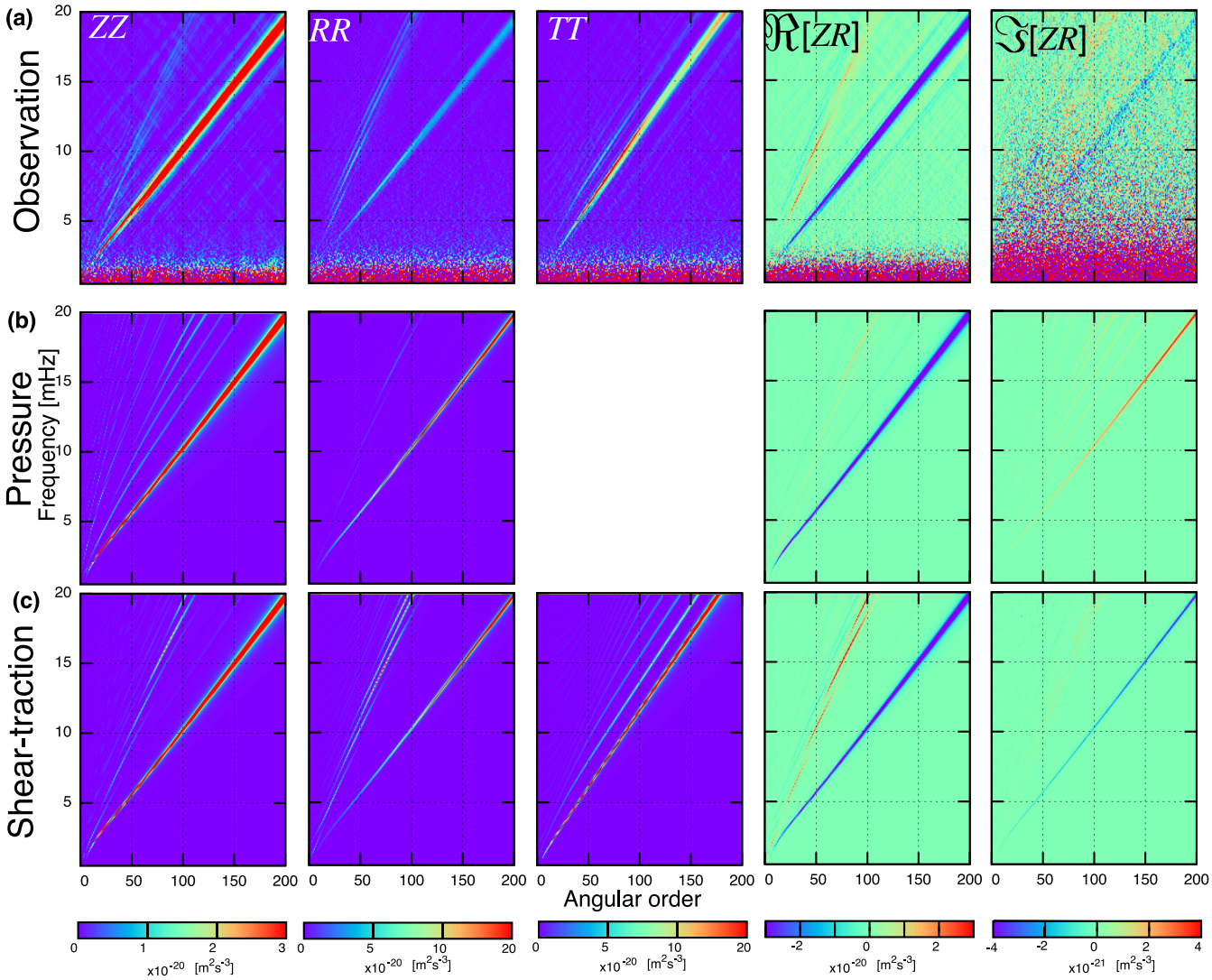

Figure 3. (a) Observed FK spectrum of ZZ ($\zeta^{\rm obs}_{l,ZZ}$), RR ($\zeta^{\rm obs}_{l,RR}$) TT ($\zeta^{\rm obs}_{l,TT}$) components, and the real and imaginary part of the ZR ($\zeta^{\rm obs}_{l,RZ}$) component against angular order l and frequency. (b) Synthetic FK spectra for pressure sources ($\zeta^{p}_{l,ZZ}$, $\zeta^{p}_{l,RR}$ and $\zeta^{p}_{l,RZ}$). The pressure source cannot explain the observed Love wave excitations or the observed overtones of spheroidal modes. The model also cannot explain the imaginary part $\Im[ZR]$. (c) Synthetic FK spectra for shear traction sources ($\zeta^{t}_{l,ZZ}$, $\zeta^{t}_{l,RR}$, $\zeta^{t}_{l,TT}$ and $\zeta^{t}_{l,RZ}$). Those for shear traction sources can explain even the observed overtones and imaginary parts of observed $\Im[ZR]$.

complete record was segmented into about 2.8-hr data with an overlap of 1.4 hr. In order to avoid the effects of large earthquakes, we discarded all the seismically disturbed segments (Nishida & Kobayashi 1999) using the global CMT catalogue (Ekström *et al.* 2012). The records were tapered with the Welch window function. The fast Fourier transform of each segment was computed with corrections for the instrument response. We calculated the cross-spectra $\Phi^{\rm obs}_{\alpha\beta,ij}(\omega)$ between every pair of different stations (ith and jth stations) for the common record segments from 3 to 20 mHz, where α and β represent a radial (R), transverse (T) or vertical (Z) component.

Then, we stacked the real parts of the cross-spectra of ZZ, TT and RR components for the 9 yr. We also calculated real and imaginary parts of the cross-spectra of the ZR component. For a better estimation of the cross-spectra, the data weighting is crucial. The data weighting depends on the noise levels of the seismogram caused by the sensors and the local site conditions. Because horizontal components are more sensitive to local site conditions, noise levels of horizontal components are orders of magnitude higher than those of vertical components at most stations. In such a case, weighting depending on data quality is important during the stacking procedure (Takeo *et al.* 2013). Details of the data weighting are shown in Appendix B.

FK spectra calculated from the observed cross-spectra (e.g. Nishida *et al.* 2002; Nishida 2013b) are useful for comparison with the synthetic ones ($\zeta^{p}_{l,ZZ}$, $\zeta^{t}_{l,ZZ}$, etc.). We calculated the observed FK spectra as follows. By assuming homogeneous and isotropic excitation of Earth's normal modes, the TT, RR, ZZ and ZR components of the cross-spectra ($\Phi^{k\omega}_{ZZ}$, $\Phi^{k\omega}_{RR}$, $\Phi^{k\omega}_{TT}$ and $\Phi^{k\omega}_{ZR}$) can be represented by a superposition of associated Legendre functions $P_{lm}(\cos\Theta)$ as a function of separation distance Θ (Nishida 2013b) as

$$\Phi^{k\omega}_{ZZ}(\Theta) = \sum_{l} \zeta^{\rm obs}_{l,ZZ}(\omega) P_l(\cos\Theta), \tag{23}$$

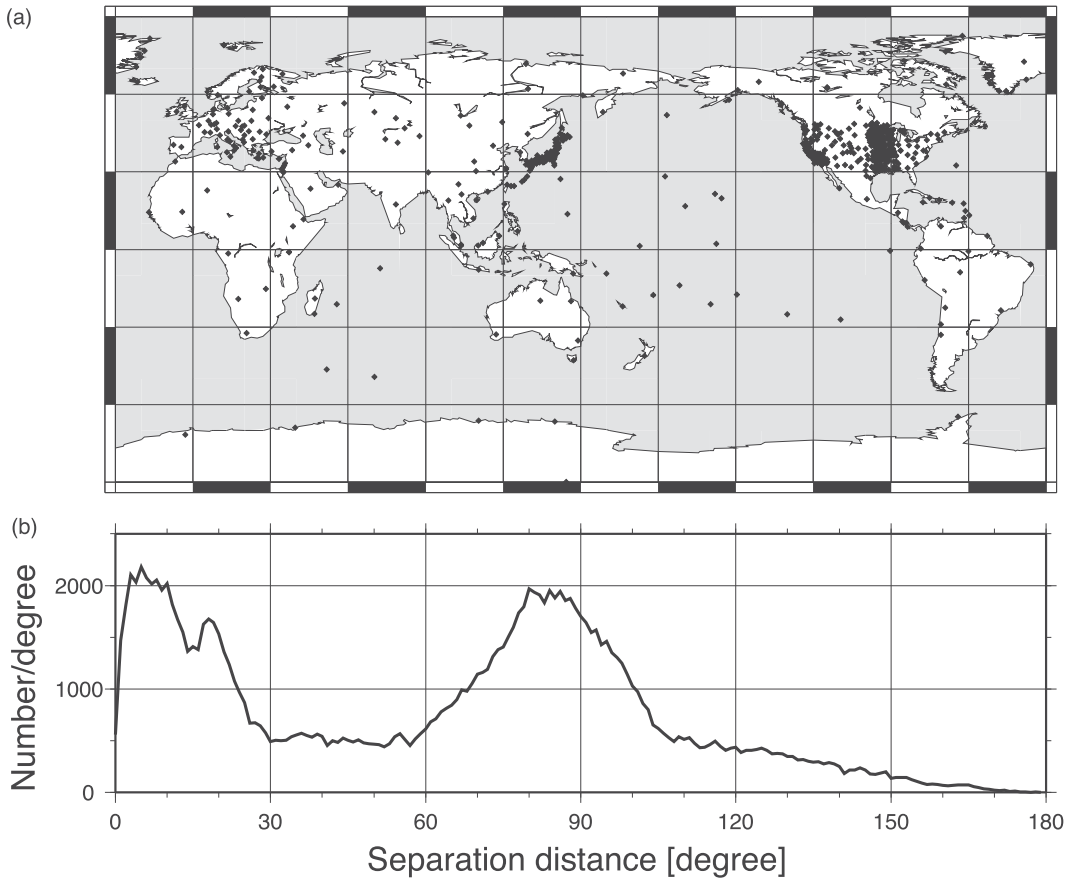

Figure 4. (a) Station distribution used in this study. We analysed seismograms from 2004 to 2011 at 618 stations with three components of broad-band seismometers (STS-1, STS2 and STS2.5) at the lowest ground noise levels. The data were retrieved from IRIS, F-net and ORFEUS data centres. (b) A histogram showing the distribution of receiver–receiver ranges for the cross-spectra. The numbers in 1° range bins are plotted as a function of range.

$$\Phi^{k\omega}_{RR}(\Theta) = \sum_l \left\{ \zeta^{\rm obs}_{l,RR}(\omega) \frac{P''_l(\cos\Theta)}{k^2} + \zeta^{\rm obs}_{l,TT}(\omega) \frac{P'_l}{k^2 \sin\Theta} \right\}, \tag{24}$$

$$\Phi^{k\omega}_{TT}(\Theta) = \sum_l \left\{ \zeta^{\rm obs}_{l,TT}(\omega) \frac{P''_l(\cos\Theta)}{k^2} + \zeta^{\rm obs}_{l,RR}(\omega) \frac{P'_l}{k^2 \sin\Theta} \right\}, \tag{25}$$

$$\Phi^{k\omega}_{ZR}(\Theta) = \sum_l \zeta^{\rm obs}_{l,ZR}(\omega) \frac{P'_l}{k}, \tag{26}$$

where l is the angular order, k is the wavenumber $\sqrt{l(l+1)}$, and the coefficients $\zeta^{\rm obs}_{l,\alpha\beta}$ represent the FK spectrum of the $\alpha\beta$ component at angular frequency ω and angular order l. This method is a natural extension of Aki's spatial autocorrelation method (Aki 1957; Haney *et al.* 2012) from a flat Earth to spherical one (see Appendix A for details). We estimated the coefficients $\zeta^{\rm obs}_{l,\alpha\beta}$ by minimizing the square differences between the synthetic cross-spectra $\Phi^{k\omega}_{\alpha\beta}$ and the observed ones $\Phi^{\rm obs}_{\alpha\beta,ij}$.

The coefficients $\zeta^{\rm obs}_{l,ZZ}$, $\zeta^{\rm obs}_{l,RR}$, $\zeta^{\rm obs}_{l,TT}$ and $\zeta^{\rm obs}_{l,ZR}$ give the FK spectra of the *ZZ*, *RR*, *TT* and *ZR* components, respectively, as shown in Fig. 3(a). The plots of the RR, ZZ and RZ components show a clear Rayleigh wave branch (fundamental spheroidal modes), whereas that of the TT component shows a Love wave branch (fundamental toroidal modes).

The figure shows that the reference model of a random shear traction source can explain the observed amplitudes of the fundamental modes, although the model overpredicted the spectral amplitudes above 10 mHz. The synthetic spectra of *RR* and *ZZ* components from the shear traction sources predict amplitudes of overtones corresponding to the shear-coupled PL waves well. The imaginary part ($\Im$) of the observed *RZ* component is also consistent with that for the shear traction source. These results suggest that random shear traction sources are dominant. However, the synthetic spectrum of the *TT* component overpredicts the observed amplitudes below 5 mHz (Fukao *et al.* 2009; Nishida 2013b). This overestimation suggests that pressure sources also contribute their excitations below 5 mHz. In order to quantify the pressure-source amplitudes, we will conduct an inversion of source spectra in the next section.

4 SOURCE INVERSION OF SEISMIC HUM

To infer the normalized source spectra of the pressure source $\bar{\Psi}^p$ and that of the shear traction source $\bar{\Psi}^t$, we fit the synthetic cross-spectra $\mathbf{\Phi}^s$ to the observed cross-spectra $\mathbf{\Phi}^{\rm obs}$ of *RR*, *TT* and *ZZ* components as

$$\mathbf{\Phi}^s(\Theta,\omega) = [\boldsymbol{K}(\Theta,\omega) * \Xi(\omega)]\,\bar{\mathbf{\Psi}}(\omega), \tag{27}$$

where

$$\mathbf{\Phi}^S(\Theta,\omega) \equiv \begin{pmatrix} \Phi_{ZZ}(\Theta,\omega) \\ \Phi_{RR}(\Theta,\omega) \\ \Phi_{TT}(\Theta,\omega) \end{pmatrix}, \qquad \bar{\mathbf{\Psi}}(\omega) \equiv \begin{pmatrix} \bar{\Psi}^p(\omega) \\ \bar{\Psi}^t(\omega) \end{pmatrix},$$

$$\boldsymbol{K}(\Theta,\omega) \equiv \begin{pmatrix} \sum_l P_l \zeta^p_{l,ZZ} & \sum_l P_l \zeta^t_{l,ZZ} \\ \sum_l \dfrac{P''_l}{k^2}\zeta^p_{l,RR} & \sum_l \left[\dfrac{P''_l}{k^2}\zeta^t_{l,RR} + \dfrac{P'_l \zeta^t_{l,TT}}{k^2 \sin\theta}\right] \\ \sum_l \dfrac{P'_l \zeta^p_{l,RR}}{k^2\sin\theta} & \sum_l \left[\dfrac{P'_l\zeta^t_{l,RR}}{k^2\sin\theta} + \dfrac{P''_l}{k^2}\zeta^t_{l,TT}\right] \end{pmatrix},$$

where $\boldsymbol{K}$ represents the corresponding components of eqs (20), and Θ_{ij} is the angle between $\boldsymbol{x}_i$ and $\boldsymbol{x}_j$.

Because the observed cross-spectrum is for the tapered records, we must take into account the effect of tapering in the synthetic cross-spectrum $\mathbf{\Phi}^s(\mathbf{x}_i, \mathbf{x}_j; \omega)$. We assume that the phases of different spectral components of seismograms are uncorrelated, because the process is random. The effect of the tapering is given by convolution with the PSD of the taper function $\Xi(\omega)$ (Welch taper used in this data analysis).

Horizontal components of broad-band seismometers record not only translational ground motions but also tilt motions in the mHz band. We also corrected the effect by a correction term $\delta_n V_l$ (Dahlen & Tromp 1998), $\delta_n V_l = -kg/(\omega^2 R_e)_n U_l$.

We determined the source spectrum $\bar{\mathbf{\Psi}}$ by minimizing the squared difference S between the observed and synthetic cross-spectra as $\partial S(\omega)/\partial \bar{\Psi}^p(\omega) = 0$, and $\partial S(\omega)/\partial \bar{\Psi}^t(\omega) = 0$. Here S is defined as

$$S(\omega) = \sum_{\alpha\beta,ij}^{i<j} \sin\Theta_{ij}\, \bar{w}_{\alpha\beta,ij} \left(\mathbf{\Phi}^{\rm obs}_{\alpha\beta,ij}(\omega) - \mathbf{\Phi}^s(\Theta_{ij},\omega)\right)^2, \tag{28}$$

where $\bar{w}_{\alpha\beta,ij}$ is the weighting of a cross-spectrum, and $\mathbf{\Phi}^{\rm obs}_{ij}$ is the vector of the observed cross-spectra,

$$\mathbf{\Phi}^{obs}_{ij}(\omega) \equiv \begin{pmatrix} \Phi^{\rm obs}_{ZZ,ij}(\omega) \\ \Phi^{\rm obs}_{RR,ij}(\omega) \\ \Phi^{\rm obs}_{TT,ij}(\omega) \end{pmatrix}. \tag{29}$$

The weighting factor $\bar{w}_{\alpha\beta,ij}$ is estimated by the standard deviation of the observed spectra divided by the square root of the stacked number (see Appendix B for details). In the summation of S, we use only the cross-spectral terms ($i \neq j$) and exclude the power-spectral terms ($i = j$) to avoid the effects of self and local seismometer noise. We also use an empirical data weighting by $\sin\Theta$ to homogenize the station distribution. This is because dense arrays such as F-net and USArray yield station pairs with separation distances shorter than 30° (Fig. 4b), and their signal levels are higher than those of distant pairs. Without the empirical weighting, the squared difference S overemphasizes the contribution of the dense arrays. Above 20 mHz, the effects of Earth's lateral heterogeneities are too strong to model the observed cross-spectra using a 1-D structure.

Fig. 5 shows the resultant source spectra of a random pressure and shear traction source. The spectrum for the shear traction source has a peak at 7 mHz, and the shear traction is dominant above 5 mHz. Above 10 mHz, no pressure source is needed to explain the observed cross-spectra. The spectra of the pressure source below 4 mHz are comparable to that of the shear traction. The spectrum of the pressure source has two local maxima, at 3.7 and 4.4 mHz, corresponding to the acoustic coupling modes (${}_0S_{29}$, ${}_0S_{37}$, respectively) between the solid Earth and the atmosphere, although the errors become larger at low frequencies. The peak amplitudes are consistent with past studies (Nishida *et al.* 2000, 2002; Kobayashi *et al.* 2008).

We estimated errors of the source spectra by a bootstrap method (Efron & Tibshirani 1994). We resampled the observed cross-spectra, allowing duplication. Fig. 5 shows standard deviations of the estimated source spectra for 100 samples. Below 4 mHz, the errors become larger because of the high noise levels of the horizontal components. Fig. 6 shows the source spectra against the spectral amplitudes of the shear traction and pressure sources at frequencies within the error ellipses. At frequencies below 4 mHz, the error ellipses are elongated along a line because of the trade-off between the shear traction and pressure sources, owing to the higher noise levels of the horizontal components.

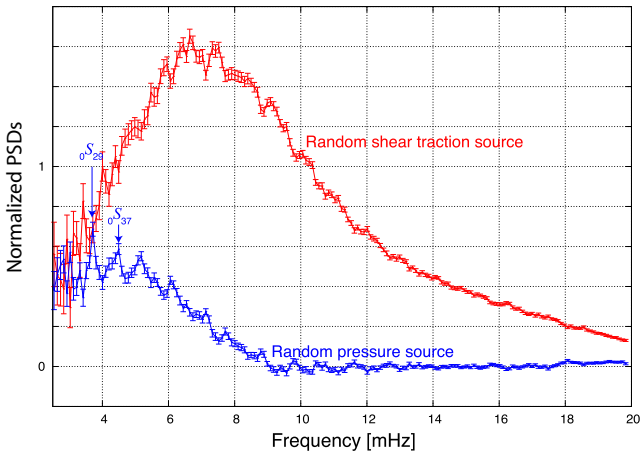

Figure 5. Power spectra of the random pressure (blue line) and shear traction (red line) sources normalized by the reference model with bootstrap errors. The pressure source spectrum shows two local maxima at 3.7 and 4.4 mHz, which correspond to acoustic coupling modes ($_0S_{29}$, $_0S_{37}$, respectively) between the fundamental spheroidal and atmospheric acoustic modes.

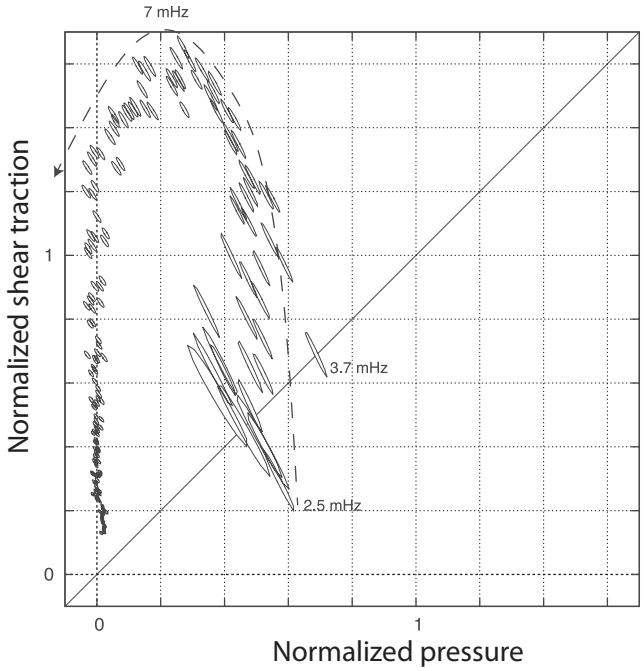

Figure 6. Plot of random pressure and shear traction against power spectral densities, with error ellipses. At frequencies below 4 mHz, the error ellipses are elongated along a line because of the trade-off between the shear traction and pressure sources, owing to the higher noise levels of the horizontal components.

5 POSSIBLE EXCITATION MECHANISMS

The observed dominance of shear traction sources above 5 mHz can be explained by topographic coupling between ocean infragravity waves and seismic surface waves (Nishida *et al.* 2008; Fukao *et al.* 2009; Nishida 2013a). This mechanism could be responsible for shear traction sources above 5 mHz. In this section, we focus on pressure sources below 5 mHz, and discuss their two possible excitation mechanisms: (1) non-linear processes of ocean waves (Webb 2007, 2008; Bromirski & Gerstoft 2009; Traer & Gerstoft 2014) and (2) atmospheric disturbances (Kobayashi & Nishida 1998; Kobayashi *et al.* 2008).

First, let us consider the excitation by ocean waves. In the frequency range 2–20 mHz, pressure changes due to the ocean gravity wave reach the ocean bottom because the wavelength becomes comparable to the ocean depth. This wave is called an ocean infragravity wave. Ocean infragravity waves propagate in the horizontal direction with a phase velocity approximately given by $\sqrt{gh}$, where g is gravitational acceleration and h is water depth. There are two types of ocean infragravity waves: edge waves (or trapped waves) and leaky waves (or freely propagating waves), as shown in Fig. 1. Slower phase velocities at shallow depths tend to trap most of the ocean infragravity waves in coastal areas (e.g. Herbers *et al.* 1995; Sheremet *et al.* 2002, 2014; Dolenc *et al.* 2005, 2008). Edge waves are repeatedly refracted and become trapped close to the shore. On the other hand, leaky waves can propagate to and from the deep ocean.

An observation at shallow depths (<100 m) showed a spectral peak for the edge waves with a nominal frequency of 4–40 mHz (Herbers *et al.* 1995). The frequency is characterized as $\sqrt{gh}$ over a typical surf zone width of L. The edge waves are generated in coastal areas, primarily by non-linear interactions of higher frequency surface gravity waves (wind waves) with dominant periods around 10 s excited by winds just above the ocean surface. Radiation stress (Longuet–Higgins & Stewart 1962) due to the wind waves with two nearly equal frequencies forces the ocean infragravity waves at the difference frequency. The radiation stress could also force the solid Earth on the ocean bottom (Traer & Gerstoft 2014). The forcing can be represented as random pressure on the ocean bottom. Non-linear mesoscale forcing by primary wind waves in the deep ocean also generates leaky waves (Uchiyama & McWilliams 2008). Peak frequencies of the leaky waves in the deep ocean range from 8 to 20 mHz (e.g. Webb 1998; Sugioka *et al.* 2010; Godin *et al.* 2013). The forcing distributed in the deep ocean may also contribute to the excitation of seismic hum as pressure sources. The radiation stress by the wind waves has higher typical frequencies, from 4 to 40 mHz, than that of the estimated random pressure source from 3 to 8 mHz. Excitation by ocean infragravity waves alone cannot explain the observed peak frequency of the pressure sources, although observations of ocean infragravity waves have been improved.

The next possible mechanism is excitation by atmospheric disturbances as shown in Fig. 1. The excitation sources can be characterized by stochastic parameters of atmospheric disturbances, the power spectra of the pressure disturbances $p(f)$, and their correlation length $L(f)$. The reference model of effective pressure given by eq. (17) is based on an ad-hoc model of atmospheric disturbances (Fukao *et al.* 2002; Nishida 2013a):

$$p(f) = 4 \times 10^3 \times \left(\frac{f}{f_0}\right)^{-2} (\mathrm{Pa^2 Hz^{-1}}),$$

$$L(f) = 600 \times \left(\frac{f}{f_0}\right)^{-0.12} (\mathrm{m}). \tag{30}$$

The model of atmospheric disturbances can explain the observed amplitudes of Rayleigh waves below 7 mHz (Nishida *et al.* 2000; Fukao *et al.* 2002; Kobayashi *et al.* 2008; Nishida 2013a), although the assumed stochastic parameters of atmospheric disturbances have large uncertainties. The uncertainty comes from the lack of global observation of atmospheric disturbances at mesoscales from 1 to 10 mHz.

The estimated pressure-source spectrum also has two local peaks, at 3.7 and 4.4 mHz, corresponding to resonant peaks of acoustic coupling between the solid Earth and the atmosphere (Watada 1995; Lognonné *et al.* 1998; Kobayashi 2007; Watada & Kanamori 2010). The two spectral peaks at acoustic coupling frequencies (${}_0S_{29}$, ${}_0S_{37}$) suggest that the excitation sources originate from atmospheric phenomena (Nishida *et al.* 2000; Kobayashi *et al.* 2008). The atmospheric disturbances should also excite background atmospheric acoustic waves in the mHz band. There are observations of such background acoustic waves excited by cumulonimbus clouds (Jones & Georges 1975) and the atmospheric turbulence in mountain regions (Bedard 1978; Nishida *et al.* 2005), although there is still no direct observation of the acoustic modes coupled with the solid Earth. On the other hand, there is no observation of the background atmospheric acoustic wave in the mHz band excited by oceanic disturbances. These facts suggest that ocean disturbances do not excite the background acoustic waves in the mHz band as in the case of microbaroms with a typical frequency of about 0.2 Hz (Donn & Naini 1973; Arendt & Fritts 2000).

In relation to background low-frequency infrasounds, background Lamb waves of Earth's atmosphere from 1 to 10 mHz were detected by array analysis of microbarometer data from the USArray in 2012 (Nishida *et al.* 2014). Lamb waves propagate non-dispersively in the horizontal direction as atmospheric acoustic waves, and are hydrostatically balanced in the vertical direction (e.g. Bretherton 1969). Because the wave energy densities decay exponentially with altitude, they are concentrated in the troposphere. The observations suggest that the most probable excitation sources are tropospheric disturbances. The tropospheric disturbances may also be responsible for excitations of background low-frequency infrasounds and seismic hum below 5 mHz as pressure sources.

Thus, the pieces of these observations suggest that the excitation mechanisms of seismic hum should be considered as a superposition of the processes of the solid Earth, atmosphere and ocean as a coupled system. To date, however, there is no unified theoretical framework that includes the excitation of Lamb waves, atmospheric acoustic waves and seismic surface waves. For further discussions, a new theory, including coupling between acoustic and Rayleigh waves, needs to be developed. Locating the pressure and shear traction sources independently is also crucial for determining the physical mechanism of the excitation sources. This is because strong pressure sources could be expected in equatorial regions with high activities of cloud convection (Shimazaki & Nakajima 2009) if the atmospheric excitation mechanism is involved. On the other hand, strong excitation could be expected in coastal regions for oceanic sources. Low signal-to-noise ratios of the horizontal components are problematic when attempting to separate the contributions of the pressure and shear traction sources. For the estimation, both data analysis and modelling methods should be developed. For the source location, the effects of Earth's lateral heterogeneities are also important, in particular above 10 mHz. Numerical methods could be effective for this application.

6 CONCLUSIONS

We developed an inversion method for estimating the source spectra of seismic hum by minimizing the squared difference between observed and synthetic cross-spectra between pairs of stations. The synthetic cross-spectra were calculated with the assumption of a spatially isotropic and homogeneous distribution of random traction sources on Earth's surface. We applied this method to the IRIS, ORFEUS and F-net records at 618 stations with three components of broad-band seismometers during the period 2004–2011. The source spectra show the dominance of shear tractions above 5 mHz, which is consistent with past studies. Below 5 mHz, however, the spectral amplitudes of pressure sources are

comparable to those of shear traction. This observation suggests that atmospheric disturbances are also probable excitation sources below 5 mHz, although ocean waves are also candidates. Thus, the excitation mechanisms of seismic hum should be considered as a superposition of the processes of the solid Earth, atmosphere and ocean as a coupled system.

ACKNOWLEDGEMENTS

I am grateful to a number of people, who have been associated with the IRIS, ORFEUS and F-net data centres from the time of the inception of these data centres, for maintaining the networks and making the data readily available. I retrieved the seismic data from the IRIS data centre using SOD software. Maps were generated using the generic mapping tools (GMT) software package. I thank the two anonymous reviewers for their constructive comments and suggestions.

REFERENCES

Aki, K., 1957. Space and time spectra of stationary stochastic waves, with special reference to microtremors, *Bull. Earthq. Res. Inst.,* **35**(3), 415–456.

Arendt, S. & Fritts, D., 2000. Acoustic radiation by ocean surface waves, *J. Fluid Mech.,* **415,** 1–21.

Bedard, A.J., 1978. Infrasound originating near mountainous regions in Colorado, *J. appl. Meteorol.,* **17,** 1014–1022.

Bensen, G.D., Ritzwoller, M.H., Barmin, M.P., Levshin, A.L., Lin, F., Moschetti, M.P., Shapiro, N.M. & Yang, Y., 2007. Processing seismic ambient noise data to obtain reliable broad-band surface wave dispersion measurements, *Geophys. J. Int.,* **69,** 1239–1260.

Berger, J., Davis, P. & Ekström, G., 2004. Ambient Earth noise: a survey of the Global Seismographic Network, *J. geophys. Res.,* **109,** B11307, doi:10.1029/2004JB003408.

Bretherton, F.P., 1969. Lamb waves in a nearly isothermal atmosphere, *Q.J.R. Meteorol. Soc.,* **95**(406), 754–757.

Bromirski, P.D. & Gerstoft, P., 2009. Dominant source regions of the Earth's hum are coastal, *Geophys. Res. Lett.,* **36**. 1–5.

Dahlen, F. & Tromp, J., 1998. *Theoretical Global Seismology,* Princeton Univ. Press, 1025 pp.

Dolenc, D., Romanowicz, B., Stakes, D., McGill, P. & Neuhauser, D., 2005. Observations of infragravity waves at the Monterey ocean bottom broadband station (MOBB), *Geochem. Geophys. Geosyst.,* **6,** Q09002, doi:10.1029/2005GC000988.

Dolenc, D., Romanowicz, B., McGill, P. & Wilcock, W., 2008. Observations of infragravity waves at the ocean-bottom broadband seismic stations Endeavour (KEBB) and Explorer (KXBB), *Geochem. Geophys. Geosyst.,* **9,** Q05007, doi:10.1029/2008GC001942.

Donn, W.L. & Naini, B., 1973. Sea wave origin of microbaroms and microseisms, *J. geophys. Res.,* **78,** 4482–4488.

Dziewonski, A.M. & Anderson, D.L., 1981. Preliminary reference Earth model, *Phys. Earth planet. Inter.,* **25,** 297–356.

Efron, B. & Tibshirani, R., 1994. *An Introduction to the Bootstrap,* Chapman & Hall.

Ekström, G., Nettles, M. & Dziewoński, A.M., 2012. The global CMT project 2004–2010: Centroid-moment tensors for 13,017 earthquakes, *Phys. Earth planet. Inter.,* **200–201,** 1–9.

Fukao, Y., Nishida, K., Suda, N., Nawa, K. & Kobayashi, N., 2002. A theory of the Earth's background free oscillations, *J. geophys. Res.,* **107**(B9), 11-1–11-10.

Fukao, Y., Nishida, K. & Kobayashi, N., 2010. Seafloor topography, ocean infragravity waves, and background Love and Rayleigh waves, *J. geophys. Res.,* **115,** B04302, doi:10.1029/2009JB006678.

Godin, O.A., Zabotin, N.A., Sheehan, A.F., Yang, Z. & Collins, J.A., 2013. Power spectra of infragravity waves in a deep ocean, *Geophys. Res. Lett.,* **40,** 2159–2165.

Haney, M.M., Mikesell, T.D., van Wijk, K. & Nakahara, H., 2012. Extension of the spatial autocorrelation (SPAC) method to mixed-component correlations of surface waves, *Geophys. J. Int.,* **191,** 189–206.

Herbers, T.H.C., Elgar, S. & Guza, R.T., 1995. Generation and propagation of infragravity waves, *J. geophys. Res.,* **100**(C12), 24863–24872.

Jones, R.M. & Georges, T.M., 1976. Infrasound from convective storms. III. Propagation to the ionosphere, *J. acoust. Soc. Am.,* **59,** 765–779.

Kobayashi, N., 2007. A new method to calculate normal modes, *Geophys. J. Int.,* **168**(1), 315–331.

Kobayashi, N. & Nishida, K., 1998. Continuous excitation of planetary free oscillations by atmospheric disturbances, *Nature,* **395,** 357–360.

Kobayashi, N., Kusumi, T. & Suda, N., 2008. Infrasounds and background free oscillations, in *Proceedings of the 8th Int. Conf. on Theoretical and Computational Acoustics,* Heraklion, Crete, Greece, 2–5 July 2007, pp. 105–114, eds Taroudakis, M. & Papadakis, P., E-MEDIA University of Crete.

Kurrle, D. & Widmer-Schnidrig, R., 2008. The horizontal hum of the Earth: a global background of spheroidal and toroidal modes, *Geophys. Res. Lett.,* **35,** L06304, doi:10.1029/2007GL033125.

Lobkis, O.I. & Weaver, R.L., 2001. On the emergence of the Green's function in the correlations of a diffuse field, *J. acoust. Soc. Am.,* **110,** 3011–3017.

Lognonné, P., Clévédé, E. & Kanamori, H., 1998. Computation of seismograms and atmospheric oscillations by normal-mode summation for a spherical earth model with realistic atmosphere, *Geophys. J. Int.,* **135,** 388–406.

Longuet–Higgins, M. & Stewart, R., 1962. Radiation stress and mass transport in gravity waves with application to surf-beats, *J. Fluid Mech.,* **13,** 481–504.

Nawa, K., Suda, N., Fukao, Y., Sato, T., Aoyama, Y. & Shibuya, K., 1998. Incessant excitation of the Earth's free oscillations. *Earth Planets Space,* **50,** 3–8.

Nishida, K., 2013a. Earth's background free oscillations, *Annu. Rev. Earth planet. Sci.,* **41,** 719–740.

Nishida, K., 2013b. Global propagation of body waves revealed by cross-correlation analysis of seismic hum, *Geophys. Res. Lett.,* **40,** 1691–1696.

Nishida, K. & Fukao, Y., 2007. Source distribution of Earth's background free oscillations, *J. geophys. Res.,* **112,** B06306, doi:10.1029/2006JB004720.

Nishida, K. & Kobayashi, N., 1999. Statistical features of Earth's continuous free oscillations, *J. geophys. Res.,* **104,** 28 741–28 750.

Nishida, K., Kobayashi, N. & Fukao, Y., 2000. Resonant oscillations between the solid Earth and the atmosphere, *Science,* **287,** 2244–2246.

Nishida, K., Kobayashi, N. & Fukao, Y., 2002. Origin of Earth's ground noise from 2 to 20 mHz, *Geophys. Res. Lett.,* **29**(10), 52-1–52-4.

Nishida, K. *et al.*, 2005. Array observation of background atmospheric waves in the seismic band from 1 mHz to 0.5 Hz, *Geophys. J. Int.,* **62,** 824–840.

Nishida, K., Kawakatsu, H., Fukao, Y. & Obara, K., 2008. Background Love and Rayleigh waves simultaneously generated at the Pacific Ocean floors, *Geophys. Res. Lett.,* **35,** L16307, doi:10.1029/2008GL034753.

Nishida, K., Kobayashi, N. & Fukao, Y., 2014. Background Lamb waves in the Earth's atmosphere, *Geophys. J. Int.,* **196**(1), 312–316.

Peterson, J., 1993. Observations and modeling of seismic background noise, U.S. Geol. Surv. Open File Rep., 93-322.

Rhie, J. & Romanowicz, B., 2004. Excitation of Earth's continuous free oscillations by atmosphere-ocean-seafloor coupling, *Nature,* **431,** 552–556.

Rhie, J. & Romanowicz, B., 2006. A study of the relation between ocean storms and the Earth's hum, *Geochem. Geophys. Geosyst.,* **7,** Q10004, doi:10.1029/2006GC001274.

Saito, T., 2010. Love-wave excitation due to the interaction between a propagating ocean wave and the sea-bottom topography, *Geophys. J. Int.,* **182**(3), 1515–1523.

Sheremet, A., Guza, T., Elgar, S. & Herbers, T.H.C., 2002. Observations of nearshore infragravity waves: seaward and shoreward propagating components, *J. geophys. Res.,* **107**(C8), 10-1–10-10.

Sheremet, A., Staples, T., Ardhuin, F., Suanez, S. & Fichaut, B., 2014. Observations of large infragravity-wave run-up at Banneg Island, France, *Geophys. Res. Lett.,* **41**(3), 976–982.

Shimazaki, K. & Nakajima, K., 2009. Oscillations of atmosphere—solid Earth coupled system excited by the global activity of cumulus clouds, *EOS, Trans. Am. geophys. Un.,* **90**(52), Fall Meet. Suppl., Abstract S23A-1734.

Suda, N., Nawa, K. & Fukao, Y., 1998. Earth's background free oscillations, *Science,* **279,** 2089–2091.

Sugioka, H., Fukao, Y. & Kanazawa, T., 2010. Evidence for infragravity wave-tide resonance in deep oceans, *Nat. Commun.,* **1,** 84.

Takagi, R., Nakahara, H., Kono, T. & Okada, T., 2014. Separating body and Rayleigh waves with cross terms of the cross-correlation tensor of ambient noise, *J. geophys. Res.,* **119,** 2005–2018.

Takeo, A., Nishida, K., Isse, T., Kawakatsu, H., Shiobara, H., Sugioka, H. & Kanazawa, T., 2013. Radially anisotropic structure beneath the Shikoku Basin from broadband surface wave analysis of ocean bottom seismometer records, *J. geophys. Res.,* **118,** 2878–2892.

Traer, J. & Gerstoft, P., 2014. A unified theory of microseisms and hum, *J. geophys. Res.,* **119,** 3317–3339.

Traer, J., Gerstoft, P., Bromirski, P.D. & Shearer, P.M., 2012. Microseisms and hum from ocean surface gravity waves, *J. geophys. Res.,* **117,** B11307, doi:10.1029/2012JB009550.

Uchiyama, Y. & McWilliams, J.C., 2008. Infragravity waves in the deep ocean: generation, propagation, and seismic hum excitation, *J. geophys. Res.,* **113,** C07029, doi:10.1029/2007JC004562.

Watada, S., 1995. Part I: near–source acoustic coupling between the atmosphere and the solid Earth during volcanic eruptions, *PhD thesis,* California Institute of Technology.

Watada, S. & Kanamori, H., 2010. Acoustic resonant oscillations between the atmosphere and the solid Earth during the 1991 Mt. Pinatubo eruption, *J. geophys. Res.,* **115,** B12319, doi:10.1029/2010JB007747.

Watada, S. & Masters, G., 2001. Oceanic excitation of the continuous oscillations of the Earth, *EOS, Trans. Am. geophys. Un.,* **82**(47), Fall Meet. Suppl., Abstract S32A-0620.

Webb, S.C., 1998. Broadband seismology and noise under the ocean. *Rev. Geophys.,* **36,** 105–142.

Webb, S.C., 2007. The Earth's 'hum' is driven by ocean waves over the continental shelves, *Nature,* **445**. 754–756.

Webb, S.C., 2008. The Earth's hum: the excitation of Earth normal modes by ocean waves, *Geophys. J. Int.,* **174,** 542–566.

Winch, D. & Roberts, P., 1995. Derivatives of addition theorems for Legendre functions, *J. Aust. Math. Soc. Ser. B 37(1995),* **37,** 212–234.

APPENDIX A: ADDITIONAL THEOREM OF VECTOR SPHERICAL HARMONICS

For the additional theorem of vector spherical harmonics, we consider the spherical triangle as shown in Fig. A1. The triangle is defined by three points (the pole, $\hat{\boldsymbol{r}}_1$, and $\hat{\boldsymbol{r}}_2$) on the sphere. We also define angles θ_1, θ_2, ϕ_1, ϕ_2, χ_1 and χ_2 as shown in Fig. A1. We note that $\cos\Theta = \cos\theta_1\cos\theta_2 + \sin\theta_1\sin\theta_2\cos(\phi_1 - \phi_2)$.

We start the additional theorem of spherical harmonics (Dahlen & Tromp 1998) as

$$\sum_{m=-l}^{l} \mathcal{Y}_{lm}(\theta_1,\phi_1)\mathcal{Y}_{lm}(\theta_2,\phi_2) = \left(\frac{2l+1}{4\pi}\right) P_l(\cos\Theta). \tag{A1}$$

Differentiation of the additional theorem with respect to the parameters θ_1 and θ_2 and use of the expressions for the derivatives of Θ, χ_1 and χ_2 gives the following additional theorem directly (Winch & Roberts 1995) as

$$\sum_{m=-l}^{l} \frac{\partial\mathcal{Y}_{lm}(\theta_1,\phi_1)}{\partial\theta_1}\mathcal{Y}_{lm}(\theta_2,\phi_2) = \left(\frac{2l+1}{4\pi}\right)\frac{\mathrm{d}P_l(\cos\Theta)}{\mathrm{d}\Theta}\cos\chi_1, \tag{A2}$$

$$\sum_{m=-l}^{l} \frac{1}{\sin\theta_1}\frac{\partial\mathcal{Y}_{lm}(\theta_1,\phi_1)}{\partial\phi_1}\mathcal{Y}_{lm}(\theta_2,\phi_2) = \left(\frac{2l+1}{4\pi}\right)\frac{\mathrm{d}P_l(\cos\Theta)}{\mathrm{d}\Theta}\sin\chi_1, \tag{A3}$$

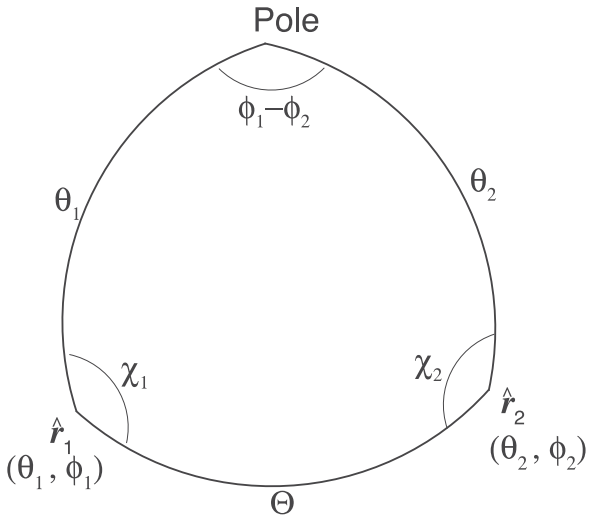

Figure A1. Spherical triangle showing nomenclature used.

$$\sum_{m=-l}^{l} \frac{\partial \mathcal{Y}_{lm}(\theta_1,\phi_1)}{\partial\theta_1}\frac{\partial \mathcal{Y}_{lm}(\theta_2,\phi_2)}{\partial\theta_2} = \left(\frac{2l+1}{4\pi}\right)\left[\frac{d^2P_l(\cos\Theta)}{\mathrm{d}\Theta^2}\cos\chi_1\cos\chi_2 - \frac{\mathrm{d}P_l(\cos\Theta)}{\mathrm{d}\Theta}\frac{\sin\chi_1\sin\chi_2}{\sin\Theta}\right], \tag{A4}$$

$$\sum_{m=-l}^{l} \frac{\partial \mathcal{Y}_{lm}(\theta_1,\phi_1)}{\partial\theta_1}\frac{1}{\sin\theta_2}\frac{\partial \mathcal{Y}_{lm}(\theta_2,\phi_2)}{\partial\phi_2} = -\left(\frac{2l+1}{4\pi}\right)\left[\frac{d^2P_l(\cos\Theta)}{\mathrm{d}\Theta^2}\cos\chi_1\sin\chi_2 + \frac{\mathrm{d}P_l(\cos\Theta)}{\mathrm{d}\Theta}\frac{\sin\chi_1\cos\chi_2}{\sin\Theta}\right], \tag{A5}$$

$$\sum_{m=-l}^{l} \frac{1}{\sin\theta_1}\frac{\partial \mathcal{Y}_{lm}(\phi_1,\phi_1)}{\partial\phi_1}\frac{1}{\sin\theta_2}\frac{\partial \mathcal{Y}_{lm}(\theta_2,\phi_2)}{\partial\phi_2} = \left(\frac{2l+1}{4\pi}\right)\left[-\frac{d^2P_l(\cos\Theta)}{\mathrm{d}\Theta^2}\sin\chi_1\sin\chi_2 + \frac{\mathrm{d}P_l(\cos\Theta)}{\mathrm{d}\Theta}\frac{\cos\chi_1\cos\chi_2}{\sin\Theta}\right]. \tag{A6}$$

For the calculation, we use the following results of partial derivatives:

$$\frac{\partial\Theta}{\partial\theta_1} = \cos\chi_1, \quad \frac{\partial\Theta}{\partial\theta_2} = \cos\chi_2, \quad \frac{\partial\Theta}{\partial\phi_1} = \sin\theta_1\sin\chi_1, \quad \frac{\partial\Theta}{\partial\phi_2} = -\sin\theta_2\sin\chi_2, \tag{A7}$$

$$\frac{\partial\chi_1}{\partial\theta_1} = -\sin\chi_1\cot\Theta, \quad \frac{\partial\chi_1}{\partial\theta_2} = \frac{\sin\chi_2}{\sin\Theta}, \quad \frac{\partial\chi_2}{\partial\theta_1} = \frac{\sin\chi_1}{\sin\Theta}, \quad \frac{\partial\chi_2}{\partial\theta_2} = -\sin\chi_2\cot\Theta. \tag{A8}$$

The additional theorem of spheroidal modes can be written as

$$\sum_{m=-l}^{l}[\boldsymbol{P}_{lm}(\hat{\boldsymbol{r}}_1)+\boldsymbol{B}_{lm}(\hat{\boldsymbol{r}}_1)]^t[\boldsymbol{P}_{lm}(\hat{\boldsymbol{r}}_2)+\boldsymbol{B}_{lm}(\hat{\boldsymbol{r}}_2)] = \frac{2l+1}{4\pi}\boldsymbol{R}_1\begin{pmatrix} P_l(\cos\Theta) & \frac{\mathrm{d}P_l(\cos\Theta)}{kd\Theta} & 0 \\ \frac{\mathrm{d}P_l(\cos\Theta)}{k\mathrm{d}\Theta} & \frac{d^2P_l(\cos\Theta)}{k^2\mathrm{d}\Theta^2} & 0 \\ 0 & 0 & \frac{dP_l(\cos\Theta)}{k^2\mathrm{d}\Theta}\frac{1}{\sin\Theta} \end{pmatrix}\boldsymbol{R}_2. \tag{A9}$$

The additional theorem of toroidal modes can be written as

$$\sum_{m=-l}^{l}\boldsymbol{C}_{lm}{}^t\boldsymbol{C}_{lm} = \frac{2l+1}{4\pi}\boldsymbol{R}_1\begin{pmatrix} 0 & 0 & 0 \\ 0 & \frac{\mathrm{d}P_l(\cos\Theta)}{k^2d\Theta}\frac{1}{\sin\Theta} & 0 \\ 0 & 0 & \frac{d^2P_l(\cos\Theta)}{k^2\mathrm{d}\Theta^2} \end{pmatrix}\boldsymbol{R}_2. \tag{A10}$$

The rotation matrices ($\boldsymbol{R}_1$, $\boldsymbol{R}_2$) are defined as

$$\boldsymbol{R}_1 = \begin{pmatrix} 1 & 0 & 0 \\ 0 & \cos\chi_1 & \sin\chi_1 \\ 0 & -\sin\chi_1 & \cos\chi_1 \end{pmatrix} \tag{A11}$$

$$\boldsymbol{R}_2 = \begin{pmatrix} 1 & 0 & 0 \\ 0 & \cos\chi_2 & \sin\chi_2 \\ 0 & -\sin\chi_2 & \cos\chi_2 \end{pmatrix}. \tag{A12}$$

Here we consider a cross-spectrum between a pair of stations at $\hat{\boldsymbol{r}}_1$ and $\hat{\boldsymbol{r}}_2$, assuming that the random elastic wavefield can be represented by superposition of spheroidal modes (e.g. Lobkis & Weaver 2001) as

$$\boldsymbol{s}(\hat{\boldsymbol{r}}) = \sum_l a_{lm}(\omega)[\boldsymbol{P}_{lm}(\hat{\boldsymbol{r}}) + \boldsymbol{B}_{lm}(\hat{\boldsymbol{r}})]. \tag{A13}$$

The cross-spectrum between two stations can be written as $\langle \boldsymbol{s}^*(\hat{\boldsymbol{r}}_1)\boldsymbol{s}(\hat{\boldsymbol{r}}_2)\rangle$, where $\langle\rangle$ represents the ensemble average. We assumed equipartition states of modes with respect to azimuthal orders and the annular order as $\langle a^*_{lm}(\omega)a_{l'm'}(\omega)\rangle = \delta_{ll'}\delta_{mm'}$. The cross-spectra can be written as superposition of eq. (A9). A similar discussion can be applied for toroidal modes. The formulations of eqs (A9) and (A10) are natural extensions of the spatial autocorrelation method (Aki 1957; Haney *et al.* 2012) from a flat Earth to a spherical one.

APPENDIX B: WEIGHTING OF CROSS-SPECTRA

When we calculate a cross-spectrum between a pair of stations, weighting the data becomes important. In the case of microseisms at frequencies around 0.1 Hz, signal levels of the elastic wavefield change with time. Typically, the signal levels vary on a timescale of 1 d, and the amplitude of the variations reaches more than one order of magnitude. In this case, spectral whitening is efficient (e.g. Bensen *et al.* 2007). In the case of seismic hum in the mHz band, the signal levels are stationary, although the local noise level is greater than the signal levels. In this case, data weighting depending on the local noise level is effective (Takeo *et al.* 2013). In particular, the noise levels of the horizontal

components are orders of magnitude greater than those of the vertical components. For the calculation of the cross-spectrum, we suppressed noisy Fourier components using data weighting as follows.

We calculated a weighted cross-spectrum $\Phi_{ij}(f)$ between the ith and jth stations at a frequency f as

$$\Phi_{ij}(f) = \frac{1}{\sum_k w_{ij}^k(f)} \sum_k w_{ij}^k(f) \tilde{u}_i^{k*}(f) \tilde{u}_j^k(f), \tag{B1}$$

where $\tilde{u}_i^k(f)$ is a Fourier spectrum of ground acceleration of the kth segment at the ith station. Here, we dropped the subscript of the $\alpha\beta$ component for simplicity. The weighting factor $w_{ij}^k(f)$ is defined as

$$w_{ij}^k(f) = \frac{1}{|\tilde{u}_i^k(f)| + w_t(f)} \frac{1}{|\tilde{u}_j^k(f)| + w_t(f)}. \tag{B2}$$

We determined the water level $w_t(f) = \sqrt{50 \times n_l(f)}$, where n_l is the New Low Noise Model (Peterson 1993) of ground acceleration. When $50 \times n_l(f)$ is smaller than the power spectra (e.g. the horizontal components), the weight simply suppresses noisy data. When the power spectral densities are comparable to $n_l(f)$ (e.g. the vertical components at the quietest sites), the weighting w_{ij}^k becomes constant.

We also evaluated the quality of the resultant $\Phi_{ij}(f)$ of the inversion by data weighting $\bar{w}_{ij}(f)$ as

$$\bar{w}_{ij}(f) = \left(\sqrt{N_{ij}(f)} \frac{N_{ij}(f)}{\sum_k w_{ij}^k(f)} \right)^2, \tag{B3}$$

where $N_{ij}(f)$ is number of stacked traces. The weighting factor $\bar{w}_{ij}(f)$ can be interpreted as the square of the reciprocal of the standard error of $\Phi_{ij}(f)$.